Frozen orbits at high eccentricity and inclination: application to Mercury orbiter

N. Delsate, P. Robutel, A. Lemaître, T. Carletti

Noname manuscript No.
(will be inserted by the editor)

Frozen Orbits at high eccentricity and inclination: Application to Mercury orbiter.

N. Delsate[1] · **P. Robutel**[2] · **A. Lemaître**[1] · **T. Carletti**[1]

Received: date / Accepted: date

Abstract We hereby study the stability of a massless probe orbiting around an oblate central body (planet or planetary satellite) perturbed by a third body, assumed to lay in the equatorial plane (Sun or Jupiter for example) using a Hamiltonian formalism.

We are able to determine, in the parameters space, the location of the frozen orbits, namely orbits whose orbital elements remain constant on average, to characterize their stability/unstability and to compute the periods of the equilibria.

The proposed theory is general enough, to be applied to a wide range of probes around planet or natural planetary satellites.

The BepiColombo mission is used to motivate our analysis and to provide specific numerical data to check our analytical results.

Finally, we also bring to the light that the coefficient J_2 is able to protect against the increasing of the eccentricity due to the Kozai-Lidov effect and the coefficient J_3 determines a shift of the equilibria.

Keywords Methods: analytical study · Stability · Long-term evolution · Kozai resonances · Frozen Orbit equilibria

1 Introduction

BepiColombo (MPO and MMO orbiters) is a joint European and Japanese space agencies mission aimed at studying the planet Mercury. The dynamics of the rotation of Mercury has been analyzed, for example, in D'Hoedt and Lemaître (2008); D'Hoedt et al. (2010); Dufey et al. (2009) ... The MPO (Mercury Planetary Orbiter) will be brought into a polar elliptical orbit around Mercury with an inclination of 88–90°, an eccentricity of 0.1632 and a semi-major axis of 3 394 km. The MMO (Mercury Magnetospheric Orbiter) will also be brought into a polar elliptical orbit with an eccentricity of 0.6679 and a semi-major axis of 8 552 km.

[1] University of Namur, Department of Mathematics Rempart de la Vierge 8, B-5000 NAMUR,BELGIUM
E-mail: nicolas.delsate@math.fundp.ac.be
[2] IMCCE, CNRS UMR8028, Observatoire de Paris/USTL/UPMC, 77 Av. Denfert-Rochereau, F-75014 Paris, France.

Actually polar orbits are very interesting for scientific missions to planetary satellites (with near polar low-altitude) or to planet (with high-eccentric high-altitude). The orbital dynamics of such space probes is governed by the oblateness (J_2 effect) of the central body around which the space probe is orbiting and the gravity field from the third body. A well-known effect of the third-body perturbation is the change in the stability of circular orbits related to orbit inclination. This effect is a natural consequence of the Kozai-Lidov resonance (Kozai 1962; Lidov 1962). Generally the final fate of such a satellite is the collision with the central body. However if the radius of the central body is small, large cyclic variations in eccentricity are possible without collision; for examples see Russell and Brinckerhoff (2009). Therefore the control of the orbital eccentricity leads to the control of the satellite lifetime.

Scheeres et al. (2001) studied near-circular orbits in a model that included both the third body's gravity and J_2. In addition San-Juan et al. (2006) studied orbit dynamics about oblate planetary satellites using a rigorous averaging method. Paskowitz and Scheeres (2006) added the effect of the coefficient J_3. These authors mainly focused their attention to an orbiter around planetary satellites especially for Europa. So they did not take into account the eccentricity of the third body and they detailed the near-circular orbits. Recently Lara et al. (2010) studied the planar elliptic restricted three-body problem including the J_2 and J_3 coefficients, using Deprit's perturbation method allowing to build a doubly averaged Hamiltonian and to provide the transformation between osculating and mean initial conditions. However they were not able to provide either the new stable horizontal equilibrium induced by the J_2 term, or the analytical formulation of the position of the equilibria and their periods.

Our purpose is to build an easy method to find a simplified Hamiltonian model, as simple as possible, which will reproduce the motion of probes orbiting an oblate central body also taking into account the third body effect with a non-null third body eccentricity. Especially we are looking for the conditions that give rise to frozen orbits. Frozen orbits are orbits that have orbital elements constant on average. These particular orbits are able to keep constant the eccentricity. Therefore in a neighbourhood of these orbits there is a stability area where even a limited control could be used to avoid the crash with the central body. Here we are interested in determining all generic frozen orbits, not only the circular equilibria. Notice that also periodic orbits can be used to find high fidelity orbits including the first order gravity effects and arbitrary order gravity field terms (Lara and Russell 2007; Russell and Lara 2007).

Besides the oblateness (J_2 gravity term) of the central body and the gravity effect of the third body, our averaged model takes also into account the eccentricity of the orbit of the third body. Moreover let us observe that our results are given in closed form with respect to the eccentricity and inclination of the probe, namely we do not perform any power series expansion; therefore, our theory applies for arbitrary eccentricities and inclinations of the space probe, and is not limited to almost-circular orbits. We can thus conclude that the theory is general enough to be applied to a wide range of probes around a planet or around a natural planetary satellite and, can be formulated and presented in a general way that allows extension of the results to other cases.

The Mercury orbiter mission (BepiColombo) is used to motivate our analysis and to provide specific numerical data to check our analytical results.

We are able to provide the location of all frozen orbits and study their stability as a function of the involved parameters, using implicit equations and graphics. Finally we give the analytical expressions of the periods at the stable equilibria.

The analytical results are verified and confirmed using dedicated numerical simulations of the complete model.

To conclude, we discuss the effect of protection of J_2 on the increase of the eccentricity due to Kozai-Lidov effect and the apparition of an asymmetry caused by the addition of the coefficient J_3.

These equilibria and their periods can be modified by including higher order terms of the gravity field. Except for resonant relations between the frequencies of the satellite and the central body, they will not change drastically the behavior of our phase space. Henceforth, the frozen orbits presented here provide good initial conditions to find periodic or frozen orbits of the full model.

2 Motivation: numerical exploration

For the purpose of our study, we consider the modeling of a space probe subjected to the influence of Mercury's gravity field (in the following sections Mercury will be denoted by "central body") and the gravitational perturbations of the Sun (noted "third body") as well as to the direct solar radiation pressure without shadowing effect. As a consequence the system of differential equations describing the probe motion is given by

$$\ddot{\boldsymbol{r}} = \ddot{\boldsymbol{r}}_{\text{pot}} + \ddot{\boldsymbol{r}}_{\odot} + \ddot{\boldsymbol{r}}_{\text{rp}}\,, \tag{1}$$

where $\ddot{\boldsymbol{r}}_{\text{pot}}$ is the acceleration induced by the Mercury's gravity field which can be expressed as the gradient of the following potential

$$U_{\text{pot}}(r,\lambda,\phi) = -\frac{\mu}{r} + \frac{\mu}{r}\sum_{n=2}^{\infty}\sum_{m=0}^{n}\left(\frac{R_p}{r}\right)^n \mathcal{P}_n^m(\sin\phi)(C_{nm}\cos\, m\lambda + S_{nm}\sin\, m\lambda)\,, \tag{2}$$

where the quantities C_{nm} and S_{nm} are the spherical harmonics coefficients of the hermeopotential. μ and R_p are respectively the gravitational constant and equatorial radius of Mercury. The quantities (r,λ,ϕ) are the hermeocentric spherical coordinates of the space probes. $\mathcal{P}_n^m$ are the associated Legendre polynomials.

The acceleration $\ddot{\boldsymbol{r}}_{\odot}$ results from the gravity interaction with the Sun and can be expressed with respect to Mercury's centre of mass:

$$\ddot{\boldsymbol{r}}_{\odot} = -\mu_{\odot}\left(\frac{\boldsymbol{r}-\boldsymbol{r}_{\odot}}{\|\boldsymbol{r}-\boldsymbol{r}_{\odot}\|^3} + \frac{\boldsymbol{r}_{\odot}}{\|\boldsymbol{r}_{\odot}\|^3}\right)\,, \tag{3}$$

where $\boldsymbol{r}$ and $\boldsymbol{r}_{\odot}$ are the hermeocentric coordinates of the space probe and of the Sun respectively. The quantity $\mu_{\odot}$ is the gravitational constant of the Sun. This acceleration can also be expressed as the gradient of the following potential:

$$U_{\odot} = \mu_{\odot}\left(\frac{1}{\|\boldsymbol{r}-\boldsymbol{r}_{\odot}\|} - \frac{\boldsymbol{r}\cdot\boldsymbol{r}_{\odot}}{\|\boldsymbol{r}_{\odot}\|^3}\right)\,. \tag{4}$$

Regarding the direct solar radiation pressure, we assume an hypothetically spherical space probe with optical properties defined by a single scalar coefficient. The albedo of Mercury is ignored and Mercury's shadowing effects are not taken into account either. Similarly, the acceleration induced by the direct solar radiation pressure is modeled by

$$\ddot{\mathbf{r}}_{\text{rp}} = C_r\, P_r\left[\frac{a_{\odot}}{\|\mathbf{r}-\mathbf{r}_{\odot}\|}\right]^2 \frac{A}{m}\,\frac{\mathbf{r}-\mathbf{r}_{\odot}}{\|\mathbf{r}-\mathbf{r}_{\odot}\|}\,, \tag{5}$$

where C_r is the adimensional reflectivity coefficient (fixed to 1 in the rest of the paper) which depends on the optical properties of the space object surface; $P_r = 4.56 \times 10^{-6}$ N/m^2 is the radiation pressure for an object located at the distance of 1 AU from the Sun; $a_\odot$ is a constant parameter equal to the mean distance between the Sun and Mercury. The coefficient A/m is the area-to-mass ratio of the space object and will be fixed to 0.01m^2/kg.

It is worth noting that we model the gravity potential of the central body only using the J_2, C_{22} and J_3 coefficients. In our implementation, we choose the highly accurate Solar System ephemeris given by the Jet Propulsion Laboratory (`JPL`) to provide the positions of the Sun and Mercury (Standish 1998). We adopt the variable step size Bulirsch-Stoer algorithm (see e.g. Stoer and Bulirsch 1980) to numerically integrate the differential equation (1). Let us note that, for the purpose of validation, we also use a second numerical integrator `DOP853` (an explicit Runge-Kutta method of order 8(5,3) with stepsize control due to Dormand & Prince (Hairer et al. 1993)).

In Figure 1 we report the results of a numerical integration of the system of equations (1) for a set of 19 600 orbits, propagated over a 200 year time span with a entry-level step size of 300 seconds. We consider a set of initial conditions defined by an eccentricity grid of 0.005 and a semi-major axis grid of 35 km, spanning the $[2600, 7600]$ km range. The other fixed initial conditions are $i_0 = 90^\circ$ for the inclination, $\Omega_0 = 67.7^\circ$ $\omega_0 = -2^\circ$ for the longitude of the ascending node and the argument of periherm, respectively; the mean anomaly at epoch is fixed to $M_0 = 36.4^\circ$ on 14 September 2019. The area-to-mass ratio $A/m = 0.01\text{m}^2/\text{kg}$. These values have been fixed by the initial conditions of BepiColombo mission found in Garcia et al. (2007).

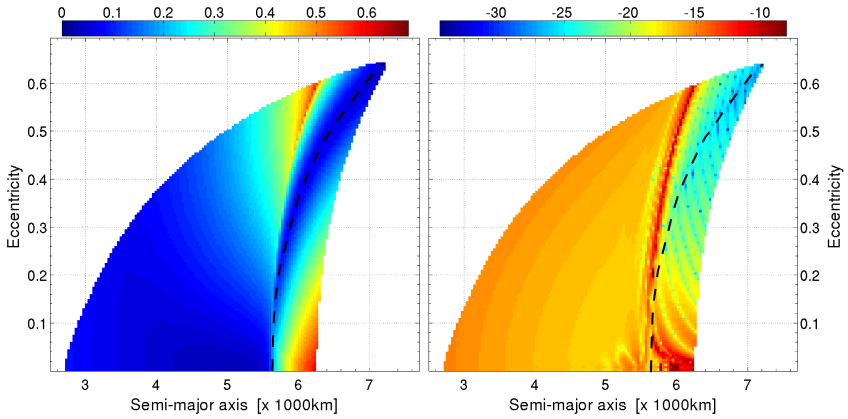

Fig. 1 The eccentricity computed as a function of the initial eccentricity e_0 and the initial semi-major axis a_0. The equations of motion include the central body attraction, the harmonics J_2, C_{22}, J_3, the solar interaction as well as the perturbing effects of the solar radiation pressure ($A/m = 0.01\text{m}^2/\text{kg}$). The eccentricity step is 0.005 and the semi-major axis step is 35 km. The initial conditions are $i_0 = 90^\circ, \Omega_0 = 67.7^\circ, \omega_0 = -2^\circ$ and $M_0 = 36.4^\circ$. The integration time is 200 years from epoch fixed at 14 September 2019. The patterns have been obtained by plotting the amplitude of variation of the eccentricity in left panel and the logarithm of the second derivative, $\log|\frac{\partial^2 \nu}{\partial k\, \partial h}|$, of the fundamental frequency of the eccentricity vector evolution in right panel.

We show the amplitude of the eccentricity (that is the difference between the maximum and minimum eccentricity reached during the integration) of each orbit in the left panel of Figure 1. For each orbit, using the Numerical Analysis of Fundamental Frequencies, for short `NAFF` (Laskar 1988, 2005), we also calculate the fundamental frequency (noted ν) of the evolution of the eccentricity vector ($k = e\cos\omega, h = e\sin\omega$). We plot the logarithm of the second derivative (noted $\log|\frac{\partial^2\nu}{\partial k\,\partial h}|$) of this frequency in the right panel of Figure 1, namely an indicator of the diffusion in the frequency space, hence also of the regularity of the orbit when it assumes small values. For more details concerning this use of frequency analysis, see Lemaître et al. (2009) where the frequency analysis has been used to study resonances in Geostationary Earth Orbits.

First, let us observe that the white zone in Figure 1 corresponds to orbits that crash onto central body's surface. Second we distinguish a curve where the variation of the eccentricity amplitude is null (dashed black line). On the right panel we plot $\log|\frac{\partial^2\nu}{\partial k\,\partial h}|$ (where ν is the fundamental frequency of the signal (k, h)) and we also distinguish on the left of the dashed black line (null-variation of eccentricity) a larger value of the log of the derivative that could correspond to a separatrix.

These structures will be analyzed and explained using a simplified model, that takes into account the central body attraction with the J_2 harmonic coefficient and the third body gravitational effect. We observed that the solar radiation pressure (for further details on the effect of direct solar radiation onto BepiColombo, we refer to Garcia et al. (2007) and Lucchesi and Iafolla (2006)) and the C_{22} coefficient do not play any role in these structures, hence these effects will be absent in the simplified model.

3 The Hamiltonian Formalism

The aim of this section is to introduce the Hamiltonian (11) already found in Tremaine et al (2009). Kepler's Hamiltonian describing the motion of a test particule orbiting an isolated point mass M is

$$\mathcal{H}_K = \frac{1}{2}v^2 - \frac{GM}{r} = -\frac{GM}{2\,a} \tag{6}$$

where G is the gravitational constant, $\boldsymbol{r}$ is the planetocentric position of the particule, $\boldsymbol{v} = \dot{\boldsymbol{r}}$, $r = |\boldsymbol{r}|$ and a is the semi-major axis of the particule.

To expand our potential, we use a vectorial method developed by Tremaine et al (2009) and used, for example, by Farago and Laskar (2010).

The quadrupole potential arising from an oblate planet ("central body") is (Eq. 2 with $n = 2$)

$$\Phi_{J_2}(\boldsymbol{r}) = \frac{GM\,J_2R_p^2}{r^3}P_2(\sin\phi) = \frac{GM\,J_2R_p^2}{r^3}P_2\Big(\cos\big(\frac{\pi}{2}-\phi\big)\Big) = \frac{GM\,J_2R_p^2}{2r^5}\Big[3(\boldsymbol{r}\cdot\boldsymbol{n}_p)^2 - r^2\Big] \tag{7}$$

where $\boldsymbol{n}_p$ is the unit vector oriented to the central body's spin axis (see Figure 2). M, R_p and J_2 are respectively the mass, the radius and the oblateness coefficient of the central body (planet or natural satellite).

We assume that $r \ll a_{3b}$ (where the subscript $_{3b}$ is related to the third body), then the potential (4) can be formulated in terms of the Legendre polynomials (where Ψ is

the planetocentric angle between the third body and the particule):

$$U_{3b} = \frac{GM_{3b}}{r_{3b}} \sum_{n\geq 2}^{\infty} \left(\frac{r}{r_{3b}}\right)^n \mathcal{P}_n(\cos\Psi) \tag{8}$$

Now, we only keep the second order Legendre polynomial ($n = 2$) and we average over the third body orbital period. So, we obtain the quadrupole in terms of the third body gravitational effect

$$\Phi_{3b}(\boldsymbol{r}) = \frac{GM_{3b}}{4a_{3b}^3(1-e_{3b}^2)^{3/2}}\left[3(\boldsymbol{r}\cdot\boldsymbol{n}_{3b})^2 - r^2\right] \tag{9}$$

where $\boldsymbol{n}_{3b}$ is the normal to the central body orbit. M_{3b}, a_{3b} and e_{3b} are respectively the mass, the semi-major axis and the eccentricity of the third body. This quadrupole term takes into account the eccentricity (e_{3b}) of the third body (e.g. Sun or Jupiter) around the central body (planet or natural satellite). Let us stress the fact that Paskowitz and Scheeres (2004); San-Juan et al. (2006); Scheeres et al. (2001) do not include this eccentricity factor in their formulation, while for a Sun-Mercury-orbiter application, this will be an important contribution.

We then average over the Keplerian orbit of the test particule described by the following elements: a semi-major axis a, an eccentricity e, and an orientation specified by the unit vectors $\boldsymbol{n}$ along the angular momentum vector, $\boldsymbol{u}$ toward the pericenter and $\boldsymbol{v} = \boldsymbol{n}\times\boldsymbol{u}$. We have (Brouwer and Clemence 1961)

$$\begin{aligned}
< r^2 > \quad &= a^2\left(1+\tfrac{3}{2}e^2\right), & \left\langle \frac{1}{r^3}\right\rangle \quad &= \frac{1}{a^3(1-e^2)^{3/2}},\\
< (\boldsymbol{r}\cdot\boldsymbol{u})^2 > &= a^2\left(\tfrac{1}{2}+2e^2\right), & < (\boldsymbol{r}\cdot\boldsymbol{v})^2 > &= a^2\left(\tfrac{1}{2}-\tfrac{1}{2}e^2\right),\\
\left\langle \frac{(\boldsymbol{r}\cdot\boldsymbol{u})^2}{r^5}\right\rangle &= \left\langle \frac{(\boldsymbol{r}\cdot\boldsymbol{v})^2}{r^5}\right\rangle \quad = \frac{1}{2a^3(1-e^2)^{3/2}}.
\end{aligned} \tag{10}$$

where $<\ \ >$ denotes the average over M, the mean anomaly of the orbit.

Let $\boldsymbol{j} \equiv \sqrt{1-e^2}\,\boldsymbol{n}$, $\boldsymbol{e} = e\boldsymbol{u}$, $\tau = \sqrt{\frac{GM}{a^3}}t$, $\varepsilon_{J2} = \frac{J_2R_p^2}{a^2}$ and $\varepsilon_{3b} = \frac{M_{3b}a^3}{Ma_{3b}^3(1-e_{3b}^2)^{3/2}}$ where $\boldsymbol{e}$ is the eccentricity vector and $\varepsilon_{J2} \geq 0$, $\varepsilon_{3b} \geq 0$. We finally define a dimensionless (divided by GM/a) Hamiltonian

$$\mathcal{K}' = -\frac{1}{2} + \frac{\varepsilon_{J2}}{4(1-e^2)^{5/2}}\left[1-e^2-3(\boldsymbol{j}\cdot\boldsymbol{n}_p)^2\right] + \frac{3\varepsilon_{3b}}{8}\left[5(\boldsymbol{e}\cdot\boldsymbol{n}_{3b})^2 - (\boldsymbol{j}\cdot\boldsymbol{n}_{3b})^2 - 2e^2\right], \tag{11}$$

That describes the secular equations of motion of a test particule around an oblate central body perturbed by the third body gravitational effect. Let us summarize the used assumptions:

1. the precession rate of the central body spin due to third body gravity is negligible;
2. the satellite is a massless test particule;
3. the third body is far enough from the central body such that the third body gravity can be approximated by a quadrupole;
4. the satellite is far enough from the central body so that the potential from the central body can be approximated as a monopole plus a quadrupole;
5. the perturbing forces ($\Phi_{J2} + \Phi_{3b}$) are weak enough so that the secular equations of motion can be used to describe the orbital motion;

6. there are not resonant relations in mean motions between the frequencies of the satellite and the frequencies of the central body.

Let us remark that San-Juan et al. (2006) already studied the orbit dynamics about planetary satellites using an extensive averaging method based on the Lie transforms to obtain averaged equations involving higher orders whose result is the introduction of an asymmetry for direct and retrograde satellite. Our simplified model will not be able to capture this asymmetry because the resulting Hamiltonian (13) will be symmetric in the satellite inclination; thus direct and retrograde satellites will have the same behavior.

Let us now make some assumptions suitable in the case of a non-inclined central body orbit (e.g. Sun-Mercury-orbiter system or Jupiter-Europa-orbiter system). We hereby consider an equatorial third body, thus $\boldsymbol{n}_p = \boldsymbol{n}_{3b}$. We also set $G = \sqrt{1-e^2}$ and $H = G\ \cos\imath$ where $\boldsymbol{j}\cdot\boldsymbol{n}_p = \sqrt{1-e^2}\ \cos\imath$. To eliminate an extra parameter, we divide the Hamiltonian by the coefficient ε_{J2} and we introduce the coefficient γ

$$\gamma = \frac{\varepsilon_{3b}}{\varepsilon_{J2}} = \frac{M_{3b}}{M a_{3b}^3 (1-e_{3b}^2)^{3/2}} \frac{a^5}{J_2 R_p^2}. \tag{12}$$

In Figure 2, we represent the geometry for the general problem (on the left) and for our simplified one (on the right).

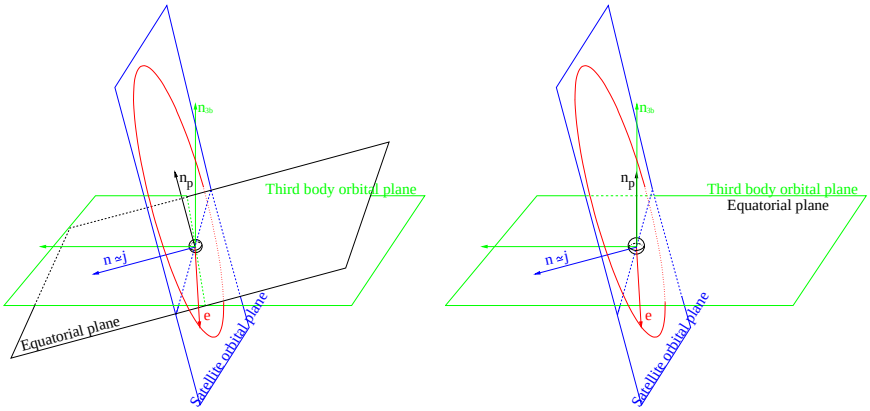

Fig. 2 Reference planes, for the general theory on the left and for our particular case on the right.

The averaged Hamiltonian is then

$$\begin{cases} \mathcal{K}' = \dfrac{\varepsilon_{J2}}{4G^3}\left(1-3\dfrac{H^2}{G^2}\right) + \dfrac{3\varepsilon_{3b}}{8}\left[5(1-G^2)\left(1-\dfrac{H^2}{G^2}\right)\sin^2\omega - H^2 - 2 + 2G^2\right] \\ \overset{\mathcal{K}'/\varepsilon_{J2}\ \text{noted by}\ \mathcal{K}}{\Longleftrightarrow} \quad \mathcal{K} = \dfrac{1}{4G^3}\left(1-3\dfrac{H^2}{G^2}\right) + \dfrac{3\gamma}{8}\left[5(1-G^2)\left(1-\dfrac{H^2}{G^2}\right)\sin^2\omega - H^2 - 2 + 2G^2\right]. \end{cases} \tag{13}$$

This one degree of freedom Hamiltonian is independent of the ascending node Ω. If we take an inclined third body, this ascending node takes place in the Hamiltonian and we

obtain a two degree of freedom problem which is non integrable. If we take $\gamma = 0$ ($\varepsilon_{3b} = 0$, namely we only take into account the oblateness effect), we have the well-known circular dynamics of the eccentricity vector due to the J_2 coefficient with an elliptical fixed point in the semi-equinoctial elements $(k, h) = (\sqrt{1-G^2}\cos\omega, \sqrt{1-G^2}\sin\omega)$. If we take $\gamma \to \infty$ ($\varepsilon_{J_2} = 0$ i.e. only the third body contribution does matter), we find the Kozai-Lidov Hamiltonian which can be found in a similar formalism in Paskowitz and Scheeres (2004) (with $e_{3b} = 0$). The Hamiltonian (13) (with $e_{3b} = 0$) can also be found in Scheeres et al. (2001).

Table 1 Connection between the semi-major axis (km) of the probe around the central body and the coefficient γ. The rows "Min.", "Missions" and "Hill" give the values of γ with respect to the semi-major axis respectively equal to the radius of the central body, to one space mission and to the radius of Hill's sphere. In the last columns, we take two particular values of γ (1/7 and 0.5) that will play a relevant role in the next sections. For Europa the minimum value of γ is 1.153, so this cell is empty.

		Min.	Missions	Hill	Particular values	
Mercury	a (km)	2 439.990	Messenger 10 136.2	175 295	4 350	5 577
	γ	0.008	9.9136	1.533×10^7	1/7	0.5
Venus	a (km)	6 051.8	Venus Express 39 176.8	1 004 270	9 350	12 010
	γ	0.008	184.485	2.042×10^9	1/7	0.5
Earth	a (km)	6 378.137	Meteosat 42 164.14	1 471 506	36 350	46 670
	γ	2.38×10^{-5}	0.30107	1.559×10^7	1/7	0.5
Mars	a (km)	3 396.190	Mars Express 9 311.95	982 748	26 150	33 580
	γ	5.288×10^{-6}	8.195×10^{-4}	1.073×10^7	1/7	0.5
Europa	a (km)	1 565.0	EJSM/JEO 3 222	13 529		
	γ	1.153	42.646	5.568×10^4		

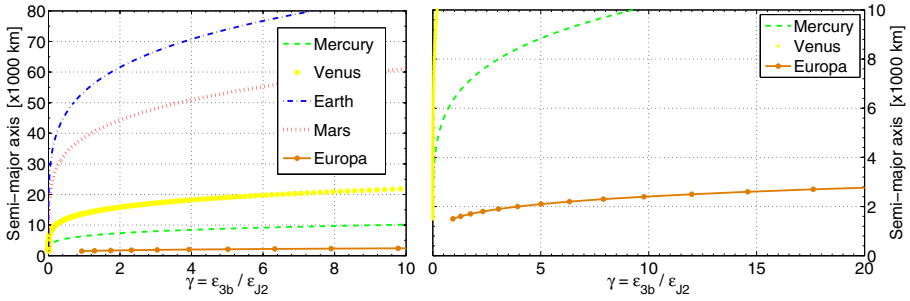

Fig. 3 Relation between γ and the semi-major axis of a test particule orbiting the central body (terrestrial planets or Europa). The third body are respectively the Sun and Jupiter.

For illustration, we show in Table 1 and draw in Figure 3 the value of the coefficient γ with respect to the semi-major axis for a probe around a terrestrial planet and around

Europa. This coefficient can be related to other parameters used in the literature. For example, it can be linked to the coefficient β in San-Juan et al. (2006), to the coefficient ϵ used in Scheeres et al. (2001) or to the coefficient $\tilde{J}_2$ in Lara et al. (2010).

4 Secular Equations of Motion

From the doubly averaged Hamiltonian (13), we obtain the equations of motion:

$$\dot{\Omega} = -H\left\{\frac{3}{2G^5} + \frac{3\gamma}{8}\left[\frac{10}{G^2}(1-G^2)\sin^2\omega + 2\right]\right\} \tag{14}$$

$$\dot{H} = 0 \tag{15}$$

$$\dot{\omega} = \frac{3\gamma}{4}\left[5\left(\frac{H^2}{G^3} - G\right)\sin^2\omega + 2G\right] + \frac{3}{4G^4}\left(5\frac{H^2}{G^2} - 1\right) \tag{16}$$

$$\dot{G} = -\frac{15\gamma}{4}(1-G^2)\left(1 - \frac{H^2}{G^2}\right)\sin\omega\cos\omega\ . \tag{17}$$

Developing these equations in eccentricity up to second order, we can obtain the equations of Scheeres et al. (2001). In the following, we will adopt a complementary approach, keeping functions of eccentricity and inclination, without power series developments, in such a way that our results hold for arbitrary eccentricities and inclinations.

From the previous set of equations, we observe that $H^2 = G^2\cos^2\imath$ is a constant of motion as in the Kozai-Lidov effect (Kozai 1962; Lidov 1962). Besides, let us remark that $0 \leq G \leq 1$, thus $0 \leq H \leq G \leq 1$ and moreover $\gamma > 0$. The first equation (14) is equal to zero only for $H = 0$ corresponding to exact polar inclination. Moreover the ascending node does not affect any of the other orbital elements. The last equation (17) equals to zero for $G = 1$, $\omega = k\pi/2,\ k \in \mathbb{N}$ or $H = G$, namely $\imath = 0°$, that is the planar case. The third equation (16) could equal to zero for $\omega = 0, \pi$ or $\omega = \pm\pi/2$. We analyze these equations in next section to find the equilibria.

5 Frozen Orbit Solutions

A frozen orbit is characterized by no secular change in orbital eccentricity and argument of pericenter. It has constant values of e, $\imath$ and ω on average, this results in fixed geometrical size and locations, apart from short period oscillations.

We have already observed that equilibria appear when $G = 1$ or $\omega = 0, \pi$ or $\omega = \pm\pi/2$. We separatly deal with these three different cases. For each of them, we give the number of equilibria, the conditions of existence and we calculate their stability.

We do not deal with the singularity $G = 0$ ($\Leftrightarrow e = 1$) because it corresponds to an escape of the orbiter. We will show that the equilibrium $G = 1$ always exists. So to begin, we deal with the non-circular case $G \neq 1$ (eccentricity $\neq 0$).

5.1 Non-circular case $G \neq 1$ (eccentricity $\neq 0$)

5.1.1 Vertical equilibria – Kozai-Lidov equilibria: $\cos\omega = 0 \Leftrightarrow \omega = \pm\pi/2$

The conditions to simultaneously equal to zero the equations (16) and (17) is:

$$\begin{cases} H^2 = \dfrac{G^2}{5}\ \dfrac{1+3G^5\gamma}{1+G^3\gamma} \\ \cos\omega = 0 \end{cases} \tag{18}$$

Because $0 \leq G < 1$ then the first equation of (18) implies that

$$H^2 < \frac{1+3\gamma}{5\gamma+5}\,. \tag{19}$$

Let us observe that this is also the value of H^2 for which one real root does exist. If this condition is violated then no real root exists.
Actually we determine[1] a region[2] given by the implicit equation

$$\begin{cases} 864\,000\,H^{16}\gamma^6 \;+\; \Big(2\,963\,520\,H^{12} \;-\; 1\,024\,H^{10}\Big)\gamma^4 \\ \qquad\qquad +\Big(1\,512\,630\,H^8 \;-\; 13\,965\,H^6 \;-\; 22\,235\,661\,H^{10}\Big)\,\gamma^2 \;+\; 12 \;=\; 0 \\ \text{and} \quad H^2 \leq \frac{1}{3087} \end{cases} \tag{20}$$

where it is possible to find three real roots. We will show that these three reals roots appear for eccentricities larger than 0.996 59. Being a case close to an escape of the orbiter, we will leave to section 7.3.3 a discussion of this "local deformation".

If the oblateness term is neglected ($\varepsilon_{J_2} \simeq 0 \Leftrightarrow \gamma \to \infty$), the existence condition becomes independent of the physical parameter and reduces to $\sin^2\imath < \frac{2}{5}$ or $\arccos\sqrt{\frac{3}{5}} \simeq 39.23^\circ \leq \imath \leq 144.77^\circ$ which corresponds to Kozai-Lidov critical inclination.

We also analyze the stability of these equilibria (18). The Jacobian of the Hamiltonian (13) evaluated at the equilibrium (18) (noted by $|_{\text{Eq.(18)}}$ or G_{kl} being the value of G at the Kozai-Lidov equilibrium) is given by:

$$\begin{cases} \dfrac{\partial^2\mathcal{K}}{\partial G^2}\Big|_{\text{Eq.(18)}} &= \dfrac{3}{2G^5}\left(2-15\dfrac{H^2}{G^2}\right) - \dfrac{9\gamma}{4}\left(1+5\dfrac{H^2}{G^4}\right)\Big|_{\text{Eq.(18)}} \\ &= \dfrac{3}{4G_{kl}^5}\ \dfrac{1}{1+\gamma G_{kl}^3}\Big(-2+\gamma G_{kl}^3 - 21\gamma G_{kl}^5 - 12\gamma^2 G_{kl}^8\Big) \\ \dfrac{\partial^2\mathcal{K}}{\partial\omega^2}\Big|_{\text{Eq.(18)}} &= -\dfrac{15}{4}\gamma(1-G^2)\left(1-\dfrac{H^2}{G^2}\right)\Big|_{\text{Eq.(18)}} \\ &= -\dfrac{3}{2}\gamma(1-G_{kl}^2)\left(\dfrac{2-G_{kl}^5\gamma}{1+G_{kl}^3\gamma}\right) \\ \dfrac{\partial^2\mathcal{K}}{\partial G\,\partial\omega}\Big|_{\text{Eq.(18)}} &= \dfrac{\partial^2\mathcal{K}}{\partial\omega\,\partial G}\Big|_{\text{Eq.(18)}} = 0. \end{cases} \tag{21}$$

[1] This can be done calculating the discriminant of the polynomial given by the first eq. 18 to find the roots (G).

[2] This region is the (G) zone in Figure 13.

In the equations (21), the term $\left.\frac{\partial^2 \mathcal{K}}{\partial \omega^2}\right|_{\text{Eq.(18)}}$ is always strictly negative (if $G < 1$). Then the equilibrium is a stable point if

$$\left.\frac{1}{G^5}\left(2 - 15\frac{H^2}{G^2}\right) - \frac{3\gamma}{2}\left(1 + 5\frac{H^2}{G^4}\right)\right|_{\text{Eq.(18)}} < 0 \Longleftrightarrow -2 - 21\gamma G_{kl}^5 + 15\gamma G_{kl} H^2 < 0\ . \tag{22}$$

This equation (22) is always satisfied for all $\gamma > 0$, $H^2 < \frac{1+3\gamma}{5\gamma+5}$ and $G_{kl} < 1$ ($e_{kl} > 0$). Therefore, for these conditions, we have two opposite stable points at $\omega = \pm\pi/2$ and G such that $H^2 = \frac{G^2}{5}\,\frac{1+3G^5\gamma}{1+G^3\gamma}$.

For the inclination $\imath = 90^\circ$ ($H^2 = 0$) the equilibrium exists for the particular value of $G = 0$ ($e = 1$). This case is only theoretical and should not be considered, because it would correspond to an escape of the orbiter. In Figure 4 we give the location of the equilibria G (18) in the parameter space (γ,H^2).

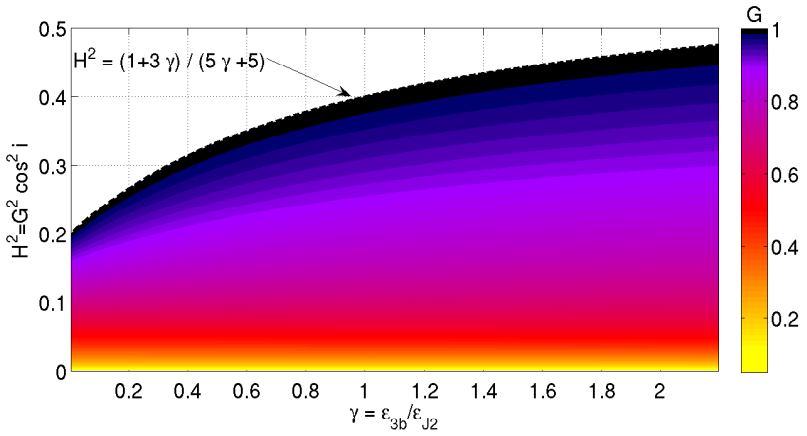

Fig. 4 Values of G at Kozai-Lidov stable (Eqs. 18 and 19) equilibria (vertical equilibria: $\omega = \pm\pi/2$) computed as a function of H^2 and γ. These equilibria are always stable. The color code indicates the value of G at the equilibrium.

5.1.2 Horizontal equilibria: $\sin\omega = 0 \Leftrightarrow \omega = 0, \pi$

The conditions to simultaneously equal to zero the equations (16) and (17) are:

$$\begin{cases} H^2 = \dfrac{G^2}{5}\ (1 - 2G^5\gamma) \\ \sin\omega = 0. \end{cases} \tag{23}$$

Using *"Le théorème d'algèbre de Sturm"* (Sturm 1835) we calculate the number of roots (G) in the range $0 \leq G < 1$ of the equation (23) as a function of the parameters γ and H^2. For $\gamma > 0$ this equation has

- one real root, equal to 0 if $H^2 = 0$ and $\gamma < 1/2$.
- three real roots (one equal to 0 and the other two opposite) if $H^2 = 0$ and $\gamma \geq 1/2$.

- three real roots (one equal to 1 and the other two opposite) if $0 < H^2 < \frac{1-2\gamma}{5}$;
- five real roots (one equal to 1 and the other ones opposite two by two) if $\gamma \geq 1/7$ and $\frac{1-2\gamma}{5} < H^2 < \frac{(7\gamma)^{-2/5}}{7}$;
- one real root equal to 1 otherwise.

In Figure 5, we give the location of the equilibria G (23) in the space (γ,H^2). The particular case $G = 1$ will be treated in the next section. We can also analyze the stability of these equilibria (23). The Jacobian of the Hamiltonian (13) evaluated at the equilibrium (23) (noted by $|_{\text{Eq.(23)}}$ or G_{hor}, being G_{hor} the value of G at the equilibrium) is given by:

$$\left\{\begin{array}{lll} \left.\dfrac{\partial^2\mathcal{K}}{\partial G^2}\right|_{\text{Eq.(23)}} & = & \left.\dfrac{3}{2G^5}\left(2-15\dfrac{H^2}{G^2}\right)+\dfrac{3\gamma}{2}\right|_{\text{Eq.(23)}} \\ & = & \dfrac{3}{2G_{hor}^5}\Big(-1+7\gamma G_{hor}^5\Big) \\ \left.\dfrac{\partial^2\mathcal{K}}{\partial \omega^2}\right|_{\text{Eq.(23)}} & = & \left.\dfrac{15}{4}\gamma(1-G^2)\left(1-\dfrac{H^2}{G^2}\right)\right|_{\text{Eq.(23)}} \\ & = & \dfrac{3}{2}\gamma(1-G_{hor}^2)(2+G_{hor}^5\gamma) \\ \left.\dfrac{\partial^2\mathcal{K}}{\partial G\,\partial \omega}\right|_{\text{Eq.(23)}} & = & \left.\dfrac{\partial^2\mathcal{K}}{\partial \omega\,\partial G}\right|_{\text{Eq.(23)}} = 0. \end{array}\right. \tag{24}$$

In the equations (24), the term $\left.\frac{\partial^2\mathcal{K}}{\partial\omega^2}\right|_{\text{Eq.(23)}}$ is always strictly positive (if $G < 1$). Then the equilibrium is a stable point if

$$\gamma > \frac{1}{G^5}\left(15\frac{H^2}{G^2}-2\right) \Longleftrightarrow G_{hor}^5 > \frac{1}{7\gamma}. \tag{25}$$

Using this equation at the equilibrium (23), we obtain conditions for stability of the stable point ($G \neq 1 \Leftrightarrow e \neq 0$)

$$\left\{\begin{array}{l} \dfrac{1-2\gamma}{5} < H^2 < \dfrac{1}{7}\left(\dfrac{1}{7\gamma}\right)^{2/5} \\ \text{and} \quad \dfrac{1}{7} \leq \gamma\,. \end{array}\right. \tag{26}$$

So the condition to have an unstable equilibrium is given by

$$\gamma < \frac{1}{7} \quad \text{or} \quad H^2 < \frac{1-2\gamma}{5} \quad \text{or} \quad H^2 > \frac{1}{7}\left(\frac{1}{7\gamma}\right)^{2/5}. \tag{27}$$

In the Figure 5, we notice that when both unstable and stable equilibrium exist, the unstable equilibrium always appears for a value of G lower than that of the stable point (i.e. for a value of e greater than the one for the stable point).

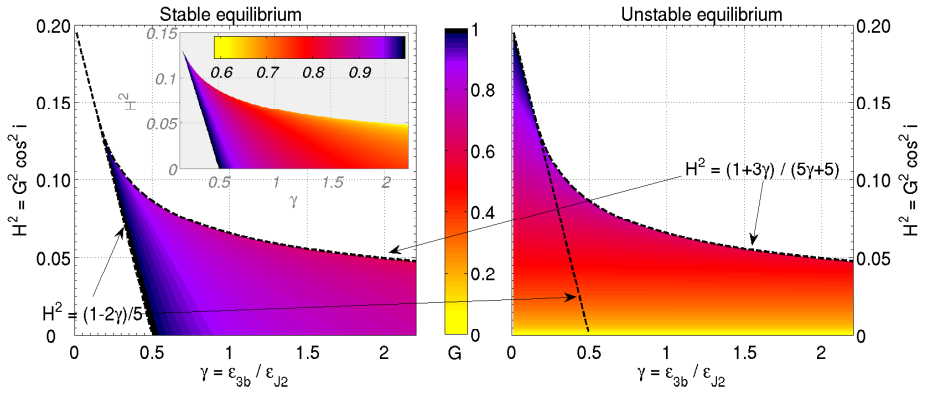

Fig. 5 Value of G at stable (on the left) (Eqs. 24 and condition 26) equilibrium and unstable (on the right) (Eqs. 24 and condition 27) equilibrium, computed as a function of H^2 and γ. The color code indicates the value of G at the equilibrium (horizontal equilibria: $\omega = 0, \pi$). The inset on the left panel shows the same plot of left panel but using a wider color code.

5.2 Circular case $G = 1$ (eccentricity $e = 0$)

For the case $G = 1$, we can use a canonical transformation to cartesian coordinates

$$x = \sqrt{1 - G^2}\sin\omega \qquad y = \sqrt{1 - G^2}\cos\omega \tag{28}$$

The new Hamiltonian is therefore

$$\begin{aligned}\mathcal{K} = \frac{1}{4}\left(\frac{1}{(1-x^2-y^2)^{3/2}} - \frac{3H^2}{(1-x^2-y^2)^{5/2}}\right)\\ + \frac{3\gamma}{8}\left[5x^2\left(1 - \frac{H^2}{1-x^2-y^2}\right) - H^2 - 2x^2 - 2y^2\right]\end{aligned} \tag{29}$$

for which it is obvious that $(0, 0)$ is always an equilibrium point whose stability can be studied computing the second derivatives and evaluate them at this equilibrium:

$$\begin{cases} \left.\dfrac{\partial^2\mathcal{K}}{\partial x^2}\right|_{x=0=y} &= \dfrac{3}{4}(1-5H^2) + \dfrac{3\gamma}{4}(3-5H^2) \\ \left.\dfrac{\partial^2\mathcal{K}}{\partial y^2}\right|_{x=0=y} &= \dfrac{3}{4}(1-5H^2) - \dfrac{3\gamma}{2} \\ \left.\dfrac{\partial^2\mathcal{K}}{\partial x\,\partial y}\right|_{x=0=y} &= \left.\dfrac{\partial^2\mathcal{K}}{\partial y\,\partial x}\right|_{x=0=y} = 0\,. \end{cases} \tag{30}$$

So, the condition to have a stability point at $x = 0 = y$ is

$$H^2 < \frac{1-2\gamma}{5} \qquad \text{or} \qquad H^2 > \frac{1+3\gamma}{5\gamma+5}\,; \tag{31}$$

and thus the condition to have an unstable point at $x = 0 = y$ is

$$\frac{1-2\gamma}{5} < H^2 < \frac{1+3\gamma}{5\gamma+5}\,. \tag{32}$$

5.3 Summary of the phase space

In this section we summarize the topology of the various possible phase spaces as a function of the parameters. We draw (Fig. 6) the bifurcation lines (conditions 19, 26 and 31) in the parameter space (γ,H^2). This bifurcation diagram is equivalent to the upper part of the bifurcation diagram in San-Juan et al. (2006) but here we draw the bifurcation lines in the general (not linked to a particular central body) space (γ,H^2). Let us observe that the bifurcation diagram presented in figure 3 of Lara et al. (2010) shows only the conditions (31) because authors were only interested in circular orbits (when $J_3 = 0$).

The $H^2 = (7\gamma)^{-2/5}/7$ line stops at the limit $\gamma = 1/7$. For this value, this curve coincides with the $H^2 = (1 - 2\gamma)/5$ condition. For the Jupiter-Europa-orbiter system, the minimum value of γ is 1.153 (Tab. 1). Therefore the phase spaces (A) and (E') do not exist.

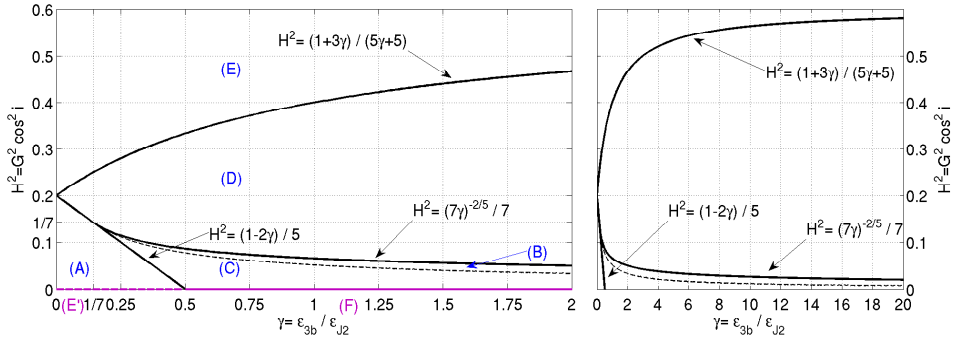

Fig. 6 Bifurcation lines and regions in the parameter space (γ,H^2). In the regions (B) and (C) we have the same number and the same stability of the equilibria but the phase space is topologically different. These regions are separated by the dashed line implicitly given by equation (33). For each region there are stable and/or unstable point(s). To visualize these points, see Fig. 7.

The region (E') and (F) in magenta color correspond to exact polar orbits ($\imath = 90^\circ$ thus $H^2 = 0$).

For each region, we attribute a letter and we draw (Fig. 7) a generic contour plot of the Hamiltonian (13) in the $(k, h, \imath)$ physical space. We recall that the motion of the inclination $\imath$ is given by the conservation of the first integral $H = G \cos\imath$. We also draw the projection of these phase spaces in the semi-equinoctial elements space $(k, h) = (\sqrt{1 - G^2}\cos\omega, \sqrt{1 - G^2}\sin\omega)$. In this phase space, it is easier to bring to the fore the stable (green point) and unstable (red cross) equilibria. The (E') phase space is trivial, containing only concentric circles in the $\imath = 90^\circ$ plane, so we do not repoduce it.

In the Figure (7), we notice that the maximum inclination is always reached at $e = 0$. This is explained by the relation $H^2 = \sqrt{1 - e^2}\cos\imath$. This last relation also gives a maximum bound onto the eccentricity: $e \leq \sqrt{1 - H^2}$. Therefore there are some values of H for which the phase space is visibly restricted in eccentricity. Beyond this eccentricity, the motion is physically impossible.

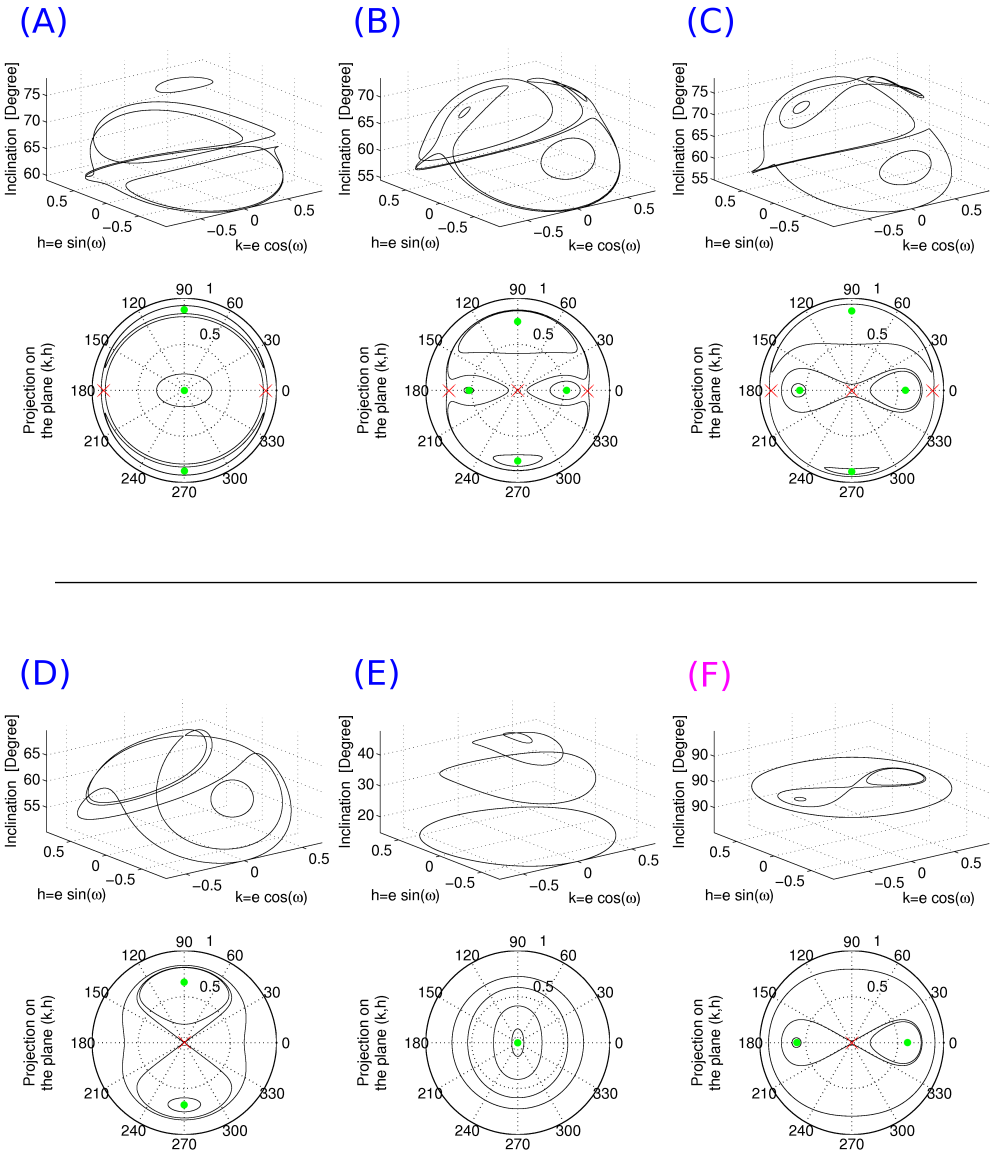

Fig. 7 Examples of some generic contour plots of the Hamiltonian (13) in $(k, h, \imath)$ space for each region of Fig. 6. The inclination $\imath$ is given in degrees and the semi-equinoctial elements (k, h) are given by $(k, h) = (\sqrt{1-G^2}\cos\omega, \sqrt{1-G^2}\sin\omega)$. The green point and red cross are respectively the stable and unstable points. In the polar projection, the radius is the eccentricity e and the angle is the pericenter ω in degrees.

Let us observe that the region near the stable equilibria allows designers to control the variation of the eccentricity even for high eccentricity. We also remark that there are "dangerous" portions of phase space such as the region around the $\gamma = H^2 = 1/7$ or near of the (B)-(C) transition. In these regions the dynamics (in a full model) could strongly change for a small variation of (H^2, γ) or (e, ω).

The transition between (B) and (C) phase spaces arises when the energy of the separatrix at the $(0, 0)$ equilibrium is equal to the energy of the unstable exterior horizontal equilibrium. This condition gives a new "fictitious" bifurcation line (dashed line in Figure 6) in the parameter space (γ, H^2). To find this line, we evaluate the Hamiltonian (13) at the unstable equilibrium $H^2 = \frac{G^2}{5}(1-2G^5\gamma)$ (Eq.23 and condition 27) and we denote this value by $\mathcal{K}_1$. Afterward, we evaluate the Hamiltonian (29) at the unstable equilibrium $(0, 0)$ (condition 32) and denote the result by $\mathcal{K}_2$. We now assume these two equilibria have the same value of Hamiltonian $\mathcal{K}$ and of H^2. Then we can replace H^2 by $\frac{G^2}{5}(1 - 2G^5\gamma)$ in $\mathcal{K}_2$ and we impose the equality between $\mathcal{K}_1$ and $\mathcal{K}_2$. Therefore we obtain the condition

$$\gamma = \frac{2 + 5G_{hor}^3 + 3G_{hor}^5}{6G_{hor}^{10} + 15G_{hor}^3 - 21G_{hor}^5} \quad \text{where } H^2 = \frac{G_{hor}^2}{5}(1 - 2G_{hor}^5\gamma) \tag{33}$$

where G_{hor} is the unstable horizontal equilibrium i.e. $H^2 = \frac{G_{hor}^2}{5}(1 - 2G_{hor}^5\gamma)$. We plot this implicit condition (33) in Figure 6 with a dashed black line. This line joins the "$(1 - 2\gamma)/5$" and "$(7\gamma)^{-2/5}/7$" lines at the $(\gamma = 1/7, H^2 = 1/7)$ point.

For the particular case $\gamma \to 0$ (J_2 effect only), we obtain, for all H^2, a phase space with circular motion of the eccentricity. We see that near to value $H^2 = 1/2$ (corresponding to the Molniya[3] critical inclination equal to 63.43° with $G = 1$; for more informations about critical inclination for a massive satellite refer to Breiter and Elipe 2006), the phase spaces (A), (D) and (E) always exist until γ becomes exactly equal to 0. In the opposite case, $\gamma \to \infty$ (third body effect only), the curve $H^2 = (7\gamma)^{-2/5}/7$ converges to 0 and the curve $H^2 = (1 + 3\gamma)/(5\gamma + 5)$ converges to 3/5 (corresponding to the Kozai-Lidov critical inclination equal to 39.23° with $G = 1$). Then only the following phase spaces are realizable: (E) (for $H^2 > 3/5$), (D) (for $0 < H^2 < 3/5$) and (F) (for $H^2 = 0$) with (F) that degenerates to an unstable point at the center. These three phase spaces will be shown in Figure 12.

In Figure 8, we show how the stable and unstable equilibria evolve, appear and disappear in each region and during the transition between the regions. We take a vertical section in Figure 6 at $\gamma = 0.4$. This section crosses the regions (A), (C), (B), (D) and (E). We draw the value of the eccentricity at the stable (solid color lines) and unstable (dashed color lines) equilibria with respect to H^2. The vertical dashed black lines mark the boundary of the regions. The numbers give the number of equilibria with this value of e. For example, 2 in magenta dashed line means that there are two unstable equilibria with the same value of e, respectively for $\omega = 0$ and $\omega = \pi$.

At the transition between (A) and (C), the central ($e = 0$) stable point bifurcates in two horizontal stable points ($e \neq 0$ and $\omega = 0, \pi$) and one unstable point ($e = 0$). At the transition between (B) and (D), the two unstable and the two stable horizontal ($\omega = 0, \pi$) equilibria converge to the same value of e and cancel out. At the transition

[3] At this inclination, due to J_2 effect, the argument of perigee remains nearly constant for a long period of time. Molniya orbits are named after a series of Soviet/Russian Molniya communications satellites which have been using this type of orbit since the mid 1960s.

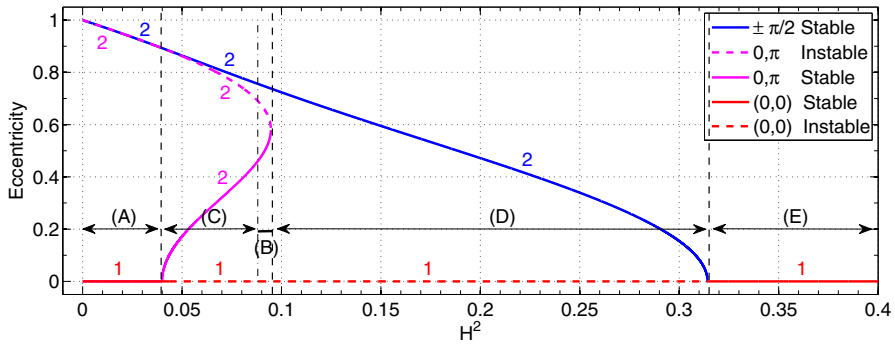

Fig. 8 For a vertical section ($\gamma = 0.4$) in the Figure 6, value of the eccentricity at unstable (dashed color lines) and stable (solid color lines) equilibria with respect to H^2. The numbers give the number of equilibria for each curve.

between (D) and (E), the two stable Kozai-Lidov equilibria ($\omega = \pm\pi/2$) come close to 0 and cancel out with the central unstable equilibrium to give one central stable equilibrium. We remark that the transition between (C) and (B) is not characterized by a change of the equilibria.

5.4 Period at the equilibrium

We are now interested in the period of the eccentricity vector at the equilibrium. This will be done by linearizing in a neighborhood of the equilibrium. Then the Hamiltonian close to the equilibrium is given by (the subscript $eq.$ means "evaluated at the equilibrium"):

$$\mathcal{K} = \mathcal{K}_{eq.} + \underbrace{\frac{\partial \mathcal{K}}{\partial G}\Big|_{eq.}}_{=0}(G - G_{eq.}) + \underbrace{\frac{\partial \mathcal{K}}{\partial \omega}\Big|_{eq.}}_{=0}(\omega - \omega_{eq.}) \tag{34}$$
$$+ \underbrace{\frac{1}{2}\frac{\partial^2 \mathcal{K}}{\partial G^2}\Big|_{eq.}}_{\stackrel{not.}{=} a}\underbrace{(G - G_{eq.})^2}_{\stackrel{not.}{=} X} + \underbrace{\frac{\partial^2 \mathcal{K}}{\partial G\,\partial \omega}\Big|_{eq.}}_{=0}(G - G_{eq.})(\omega - \omega_{eq.}) + \underbrace{\frac{1}{2}\frac{\partial^2 \mathcal{K}}{\partial \omega^2}\Big|_{eq.}}_{\stackrel{not.}{=} b}\underbrace{(\omega - \omega_{eq.})^2}_{\stackrel{not.}{=} Y}$$
$$\mathcal{K} = \mathcal{K}_{eq.} + aX^2 + bY^2\,. \tag{35}$$

This is an harmonic oscillator that can be expressed in action-angle variables (ψ, J) defined as (at a stable equilibrium, we have $ab > 0$):

$$X = \sqrt[4]{\frac{b}{a}}\sqrt{2J}\cos\psi \qquad \text{and} \qquad Y = \sqrt[4]{\frac{a}{b}}\sqrt{2J}\sin\psi\,. \tag{36}$$

Then the frequency at the equilibrium is given by

$$\dot{\psi} = \frac{\partial \mathcal{K}}{\partial J} = 2\sqrt{ab} = \sqrt{\frac{\partial^2 \mathcal{K}}{\partial G^2}\Big|_{eq.}\frac{\partial^2 \mathcal{K}}{\partial \omega^2}\Big|_{eq.}}\,. \tag{37}$$

Using the equation (37), the periods (τ) at the stable equilibria are given by:

– for horizontal equilibria: G such as Equation (23) and condition of stability (26)

$$\tau = \frac{4\pi}{3\sqrt{\frac{5}{2}\left[\frac{\varepsilon_{J2}}{G^5}\left(2-15\frac{H^2}{G^2}\right)+\varepsilon_{3b}\right]\varepsilon_{3b}(1-G^2)\left(1-\frac{H^2}{G^2}\right)}}\,; \tag{38}$$

– for vertical (Kozai-Lidov) equilibria: G such as Equation (18) and condition of stability (19)

$$\tau = \frac{4\pi}{3\sqrt{-\frac{5}{2}\left[\frac{\varepsilon_{J2}}{G^5}\left(2-15\frac{H^2}{G^2}\right)-\frac{3\varepsilon_{3b}}{2}\left(1+5\frac{H^2}{G^4}\right)\right]\varepsilon_{3b}(1-G^2)\left(1-\frac{H^2}{G^2}\right)}}\,; \tag{39}$$

– for central equilibrium ($e = 0$): $G = 1$ with condition of stability (31)

$$\tau = \frac{8\pi}{3\sqrt{\left[\varepsilon_{J2}(1-5H^2)+\varepsilon_{3b}(3-5H^2)\right]\left[\varepsilon_{J2}(1-5H^2)-2\varepsilon_{3b}\right]}}\,. \tag{40}$$

We remind that $\gamma = \varepsilon_{3b}/\varepsilon_{J2}$ and that the equations are dimensionless. Then the periods at the equilibria are given by $T_{eq.} = \sqrt{\frac{a^3}{GM}}\,\tau_{eq.}$.

For example, we apply these formula to a Mercury orbiter. The values for Mercury are $a_{3b} = 57\,909\,176.0$ km, $e_{3b} = 0.205\,630\,69$, $J_2 = 6.0 \times 10^{-5}$ (Anderson et al. 1987) and $R_p = 2\,439.7$ km (Seidelmann et al. 2007). In Figure 9 we plot the periods at the equilibria respectively for the three cases:

– on the left panel, the periods at the stable equilibrium with respect to the values of γ and H^2. The color code indicates the period of the fundamental frequency at the equilibrium;
– on the right panel, the location of the stable equilibrium in the phase space $(a, e, \imath)$ with the period in the color scale.

The color code is the same for the left and right panels and it is truncated at the value of 100 years. For a larger period, we use the black color. We notice that the time of space missions is very short compared with those periods. However these long periods are interesting because they allow to keep constant eccentricity during the mission time.

6 Comparison of analytical and numerical solutions

6.1 Comparison for all inclinations

The analytical results of the simplified model described above are checked using a precise numerical integration of the complete set of equations of motion (1). For our test, we use Mercury's orbiter mission profile, which nominally puts the spacecraft into a high eccentric polar orbit. Numerical integrations were performed with the Bulirsch-Stoer (Stoer and Bulirsch 1980) integrator. We reproduce hereby a few characteristic plots of the numerical simulations to confirm our analytical theory (see Figure 10). Similar results have been obtained for a wide range of initial frozen orbit conditions.

Figure 10 shows a very good agreement between analytical results and numerical simulations over a large time span (180 years).

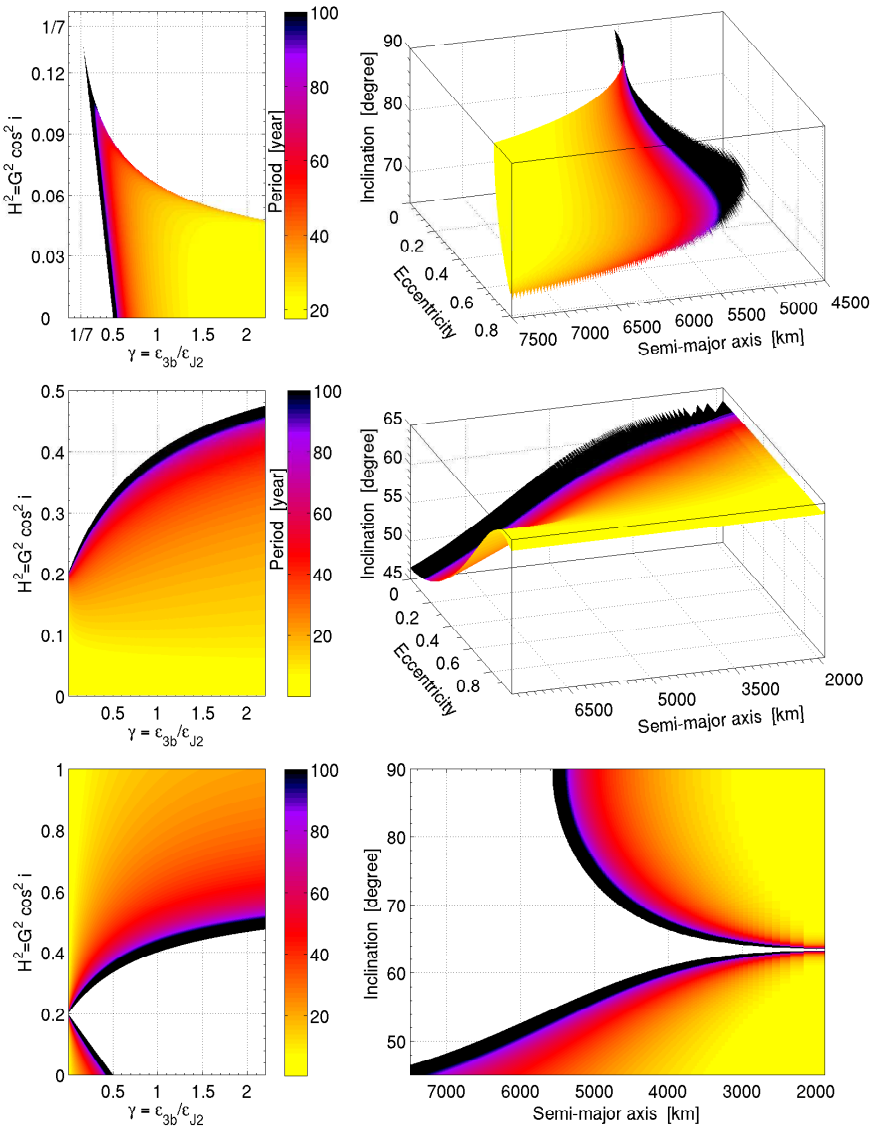

Fig. 9 Plot of the periods at the stable horizontal equilibrium (Eq. 23 with conditions 26), vertical equilibrium (Eq. 18 with condition 19) and $(0,0)$ equilibrium (with conditions 31) respectively in the upper, center and lower panels. The color code indicates the period (truncated to 100 years) of the fundamental frequency at the equilibrium. On the left panels, the period with respect to the parameters (γ, H^2). On the right panels, the location of the stable equilibrium in the physical space $(a, e, \imath)$ with its period. For the equilibrium $(0,0)$, e is always equal to 0.

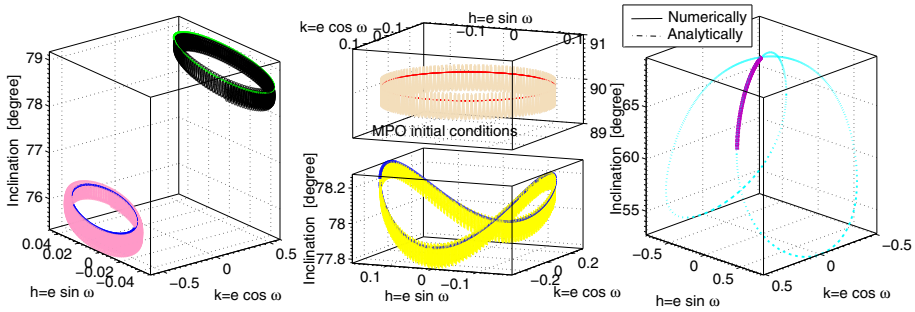

Fig. 10 Comparison between analytical and numerical results. For the left and right panel, the initial conditions are $a_0 = 6\,407$ km ($\gamma = 1.000296$), $\Omega_0 = M_0 = 0°$. In the left panel, for the lower orbit, we take $e_0 = 0.545055$ ($G = 0.8384$), $\imath_0 = 76.646989°$ ($H^2 = 3.7492 \times 10^{-2}$) and $\omega_0 = 180°$; for the upper orbit, we take $e_0 = 0.6$ ($G = 0.8$), $\imath_0 = 78.221768°$ ($H^2 = 0.26666666$) and $\omega_0 = 0°$. For the right panel, the initial conditions are $e_0 = 0.01$ ($G = 0.99995$), $\imath_0 = 69.73104°$ ($H^2 = 0.1199999$) and $\omega_0 = 0°$. For the middle panels, the initial conditions are, for the lower panel $a_0 = 4\,650$ km ($\gamma = 0.17096$), $e_0 = 0.3$ ($G = 0.9539392$), $\imath_0 = 77.89775°$ ($H^2 = 0.04$) and $\Omega_0 = M_0 = \omega_0 = 0°$; for the upper panel, we take the MMO initial conditions: $a_0 = 3\,394$ km ($\gamma = 0.0417$), $e_0 = 0.163229$ ($G = 0.986$), $\imath_0 = 90°$ ($H^2 = 0$) and $\Omega_0 = 67.7°$, $\omega_0 = 16°$, $M_0 = 0°$. The numerical model takes into account the contribution of J_2 and C_{22} and the solar gravitational effect, with starting epoch fixed at 14 September 2019. The analytical model is based on Equations (14, 16, 17). We plot the numerical integrations with continued lines and the analytical results with dashed lines. The time of the integrations is equal to 180 years. In the right panel, the numerical integration leads to a crash onto the planet after 40 years.

6.2 Comparison for polar inclination and explanation of the preliminary numerical results

In the Figure 11, we present a graphical comparison between numerical integration and analytical results (contour plots of the Hamiltonian (13)) for an exact polar inclination. We see that the analytical theory is very close to the numerical integration for all

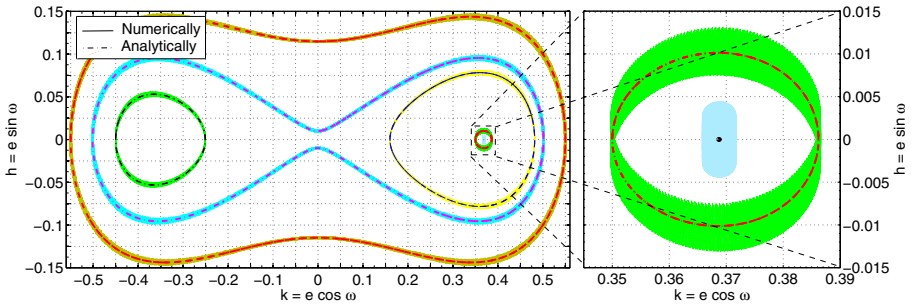

Fig. 11 Comparison between analytical and numerical results for exact polar orbiter. The initial conditions are $a_0 = 6\,000$ km ($\gamma \simeq 0.72$), $\imath_0 = 90°$, $\Omega_0 = 67.7°$, $\omega_0 = -2°$, $M = 36.4°$. The numerical and analytical model are the same of Figure 10. In dashed line the analytical result and in continued line the numerical integration. On the right a blow-up of the center of libration.

initial eccentricities. We also notice that the addition of C_{22} does not modify much the motion. Then the initial conditions of frozen orbits found by our method give good initial conditions to find frozen orbits in a full model.

In the right panel, we show two solutions close to the libration point and we see that, the closer the motion is to the libration equilibrium, the more the numerical integrations show a discrepancy with respect to the analytical results for the periherm libration: the frozen orbit of the analytical model shows no changes in eccentricity and argument of pericenter. On the contrary, the numerical orbit has short period oscillations but constant mean values of e and ω. For indication, the analytical and numerically calculated periods at this equilibrium are given in Table 2.

Figure 11 allows us to explain the behaviors already seen in our preliminary numerical exploration (Fig. 1). In Figure 11, we take different orbits with a semi-major axis equal to 6 000 km corresponding to a vertical section in Figure 1. Then, on this section, we take some values of the eccentricity such that:

- for e near to 0, in Fig. 1, we see a large value of the amplitude of variation of the eccentricity approximatively equal to 0.5 and a high value of the second derivative.
  In Fig. 11, for e equal to 0, we are on the separatrix. Therefore the eccentricity increases (roughly until 0.5) and a little shift of the initial eccentricity causes a high difference of the frequency. Thus the second derivative of the frequency is large;
- for e close to 0.37, in Fig. 1, we see that the amplitude of variation of the eccentricity decreases until 0.
  In Fig. 11, at $e = 0.37$, we find the stable point where the eccentricity is equal to a constant;
- when e moves away from 0.37 to 0.5, in Fig. 1, we see that the amplitude of variation of the eccentricity increases from 0 to 0.5 and for $e = 0.5$, the amplitude of variation of the eccentricity is maximal and the value of the second derivative is large.
  In Fig. 11, moving away from the equilibrium ($e = 0.37$) toward the separatrix ($e \simeq 0.5$) we encounter larger and larger variations in e;
- for e near to 0.55, in Fig. 1, we see that the amplitude of variation of the eccentricity is smaller than for $e \simeq 0.5$.
  In Fig. 11, for $e \simeq 0.55$, the pericenter circulates and the maximum of the amplitude of variation of the eccentricity is roughly equal to $0.55 - 0.11 = 0.44$.
- in Fig. 1, moving along the line $e = 0$, we pass from the region (F) to the region (E') at 5 577 km (Tab.1). For semi-major axis smaller than $a = 5\,577$ km, we do not cross any separatrix and the amplitude of variation of the eccentricity is small.

6.3 Frequency comparison

To obtain a second independent validation of our analytical model, we numerically compute, using the `NAFF` algorithm (Laskar 1988, 2005), the period of the numerical solutions of the full system (1) obtained through numerical integration, and we compare it with the period of the equilibrium points of the simplified model.

Table 2 provides a summary of these comparisons. We can observe a very good agreement between the two methods. Some small differences can be explained as follows:

- the exact equilibrium in the doubly averaged system is not the exact equilibrium in the full numerical model;

Table 2 Comparison between the period of the equilibria determined in the analytical model and the period numerically obtained using `NAFF`. The Horiz.* corresponds to the equilibrium in the blow-up of Fig. 11

Initial condition				Period [year]		Error
Which equi.	a [km]	e	$\imath$ [degree]	Analytical	Numerical	relative %
Kozai	5 750	0.4731	58.37	29.30	29.25	0.17
Horiz.	8 083	0.4922	77.68	35.67	35.61	0.17
Horiz.	5 818	0.5418	71.93	42.17	42.26	0.21
Horiz.*	6 000	0.369	90.00	44.576	44.528	0.11
(0,0)	3 429	0.0	47.64	9.127	9.135	0.08
(0,0)	4 731	0.0	77.01	56.594	55.274	2.38

– the full numerical model contains short period terms which disturb the long period dynamics.

The closeness of the periods found analytically as well as numerically shows also that our method can provide a very good approximation of periods and location of frozen orbits even in the full osculating model.

7 Discussions

7.1 J_2: the protector

The aim of this section is to describe the protection mechanism of the coefficient J_2 on the increase of the eccentricity. We recall that our Hamiltonian (13), once we set the coefficient $\varepsilon_{J_2} = 0$, reduces to the Kozai-Lidov Hamiltonian:

$$\mathcal{K}_{kl} = \frac{3\,\varepsilon_{3b}}{8}\left[5(1-G^2)\left(1-\frac{H^2}{G^2}\right)\sin^2\omega - H^2 - 2 + 2G^2\right]. \tag{41}$$

In the upper panels of Figure 12, we draw the possible phase spaces of this Hamiltonian. For comparison, we plot in the lower panels analogous phase spaces with Mercury's $J_2 = 6\times10^{-5}$.

In the right panels ($H^2 > 3/5$) we have a similar behavior of our (E) case (Fig. 7). For the exact polar orbits ($H^2 = 0$ in the left panel of the Fig. 12), in the Kozai-Lidov Hamiltonian (top left panel in Fig. 12), all the probes are ejected: the eccentricity always grows up to 1. Instead, with the addition of the coefficient J_2 we have (Fig. 7) the phase space (E') or (F) (in bottom left of Fig. 12 we have the E') where it is possible that the eccentricity does not increase or that it remains at a fixed value. In the middle case ($0 < H^2 < 3/5$) we see that for an initial pericenter close to 0, the eccentricity increases (top center panel in Fig. 12). Instead, in our case ($J_2 \neq 0$), the phase spaces (A), (B), (C) and (E) (Fig. 7) show that it is possible to find initial condition (other than $\omega \simeq \pm\pi/2$) where the increasing of the eccentricity is naturally controlled. Nevertheless, with the addition of the coefficient J_2, we can keep the vertical eight-shape (phase space (D) in Fig. 7 or in bottom center in Fig. 12) but with a lower increase of eccentricity.

The J_2 acts as a protection mechanism against the increase of the eccentricity due to the Kozai-Lidov effect. This mechanism also appears for planets in tight binary systems (Saleh and Rasio 2009), where the general relativistic effects become dominant and can cause the periastron to precess on very short timescales. Therefore this precession can lead to the suppression of Kozai oscillations.

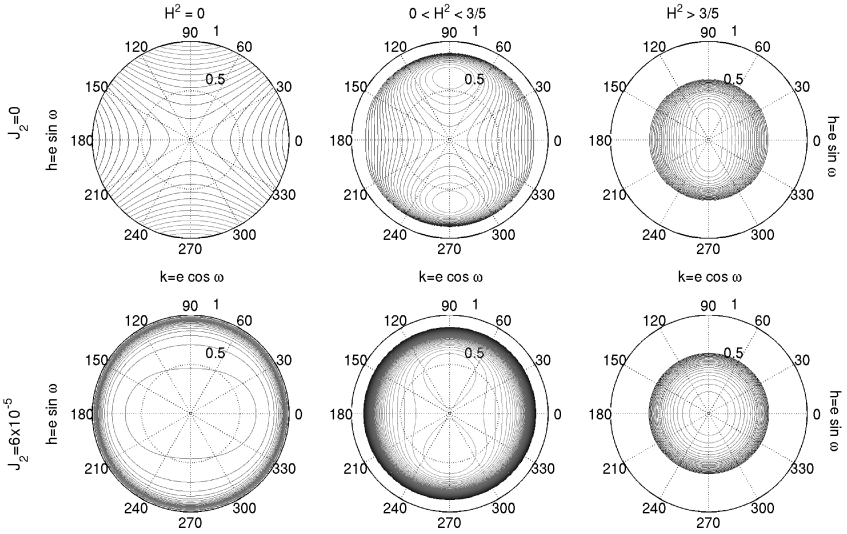

Fig. 12 In the upper panels, all possible phase spaces for Kozai-Lidov Hamiltonian (41) with respect to the values of H^2. For comparison, in the lower panels analogous phase spaces with $J_2 = 6 \times 10^{-5}$ adapted to the case of Mercury.

7.2 Local deformation of the Kozai-Lidov equilibrium

We have seen that the condition to get the Kozai-Lidov equilibrium is (Eq. 19)

$$H^2 < \frac{1+3\gamma}{5\gamma+5} \, . \tag{42}$$

Actually there is a region, where it is possible to find three real roots for G, as a function of H^2 and γ. The conditions to have these three real roots are given by:

$$KL_3 \equiv \begin{cases} 864\,000\,H^{16}\gamma^6 \, + \, \left(2\,963\,520\,H^{12} \, - \, 1\,024\,H^{10}\right)\gamma^4 \\ \qquad\qquad + \left(1\,512\,630\,H^8 \, - \, 13\,965\,H^6 \, - \, 22\,235\,661\,H^{10}\right)\gamma^2 \, + \, 12 \, = \, 0 \\ \text{and} \quad H^2 \leq \frac{1}{3087} \end{cases} \tag{43}$$

We draw the solutions of this equation, denoted by KL_3, that demarcates the region denoted (G), on the left panel of the Figure 13. Let us observe that this condition

is verified for large values of γ ($\gamma \geq 7203\sqrt{3}/2$) and for very small values of H^2 ($H^2 \leq 1/3087$). An example of the phase space is plot in Figure 13 in the middle panels. In this region, the vertical Kozai-Lidov stable equilibrium bifurcates in two stable and one unstable vertical Kozai-Lidov equilibria producing thus a local deformation of the Kozai-Lidov equilibrium. We show an example of these three equilibria in the right panels of the Figure 13. Initial conditions close to these equilibria (external orbit in the right panels of Fig. 13) give rise to orbit librating around this set of three equilibria.

It is possible to find that this bifurcation appears, in the (G) region, for a value of G smaller than $\sqrt{3}/21 \simeq 0.082\,478\,6$ corresponding to a value of the eccentricity e larger than $\sqrt{438}/21 \simeq 0.996\,59$. Recalling the formula $H = G\cos\imath$, we obtain a minimal inclination of 87.27°. Nevertheless for the Sun-Mercury-orbiter application these conditions lead orbiters to crash onto Mercury.

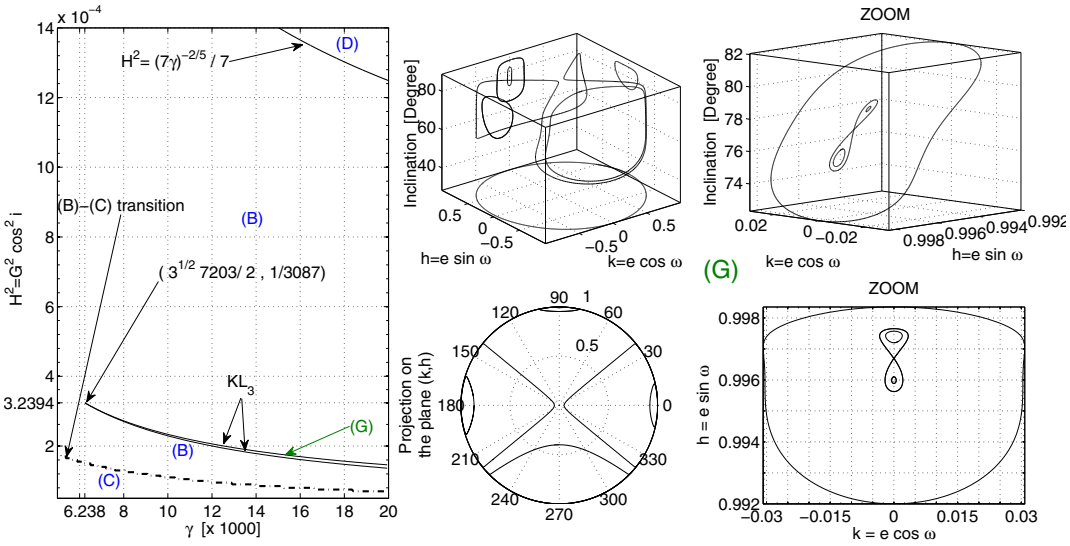

Fig. 13 Local deformation of the Kozail-Lidov equilibrium. The bifurcation lines in the left panel with the new region (G) demarcated by the two curves KL_3. Example of generic contour (for (G) region) of the Hamiltonian (13) in $(k, h, \imath)$ space in the middle panels. A zoom of the local deformation in the right panels.

7.3 J_3 discussion

In Paskowitz and Scheeres (2006) and Lara et al. (2010) the authors included the J_3 (the "*pear shape*") of the central body in their system. Paskowitz and Scheeres (2006) noticed that the coefficient J_3 caused an asymmetry between the solutions of the frozen orbits for $\omega = \pm\pi/2$ but they did not explain the reasons of this beavior. Lara et al. (2010) gived the values of the pericenter at the "horizontal" equilibria and a region (e, H) where frozen orbits may exist with $\omega \neq \pm\pi/2$.

The potential arising from a central body with a $J_3 \neq 0$ is given by

$$\Phi_{J3}(\boldsymbol{r}) = \frac{GMJ_3R_p^3}{2r^7}\ (\boldsymbol{r}\cdot\boldsymbol{n}_p)\Big[5(\boldsymbol{r}\cdot\boldsymbol{n}_p)^2 - 3r^2\Big]. \tag{44}$$

The averaged Hamiltonian is then

$$\frac{3\ GMJ_3R_p^3}{2\ a^4(1-e^2)^{5/2}}\ e\ \sin\omega\ \sin\imath\ \left(1-\frac{5}{4}\sin^2\imath\right). \tag{45}$$

It is easy to understand that the north-south asymmetrical form of J_3 induces an additional term proportional to $\sin(\imath)$ (which is not an even function) in the Hamiltonian (45). The odd powers of $(\boldsymbol{r}\cdot\boldsymbol{n}_p)$ are responsible for emergence (after average) of the $(\sin\omega\ \sin\imath)$ coefficient.

Using our variables $G = \sqrt{1-e^2}$, $H = G\cos\imath$, we can define the dimensionless (divided by GM/a) potential that we can add to the Hamiltonian (13):

$$\underbrace{\frac{J_3R_p^3}{a^3}}_{\stackrel{not.}{=}\varepsilon_{J3}}\ \frac{3}{8G^8}\sqrt{1-G^2}\ \sin\omega\ \sqrt{G^2-H^2}\ (5H^2-G^2). \tag{46}$$

Introducing the coefficient $\delta = \dfrac{\varepsilon_{J3}}{\varepsilon_{J2}} = \dfrac{J_3R_p}{J_2a}$, the equations of motion (17 and 16) can be rewritten in compact form as follows:

$$\begin{cases} \dot{G} = F_1(G,H,\gamma)\ \sin\omega\cos\omega\ +\ F_2(G,H,\delta)\ \cos\omega \\ \dot{\omega}\ = F_3(G,H,\gamma)\ +\ F_4(G,H,\gamma)\ \sin^2\omega\ +\ F_5(G,H,\delta)\ \sin\omega \end{cases} \tag{47}$$

where the functions F_1, F_3 and F_4 can be easily identified in equations (16) and (17). The functions F_2 and F_5 come from the J_3 effect and they are proportional to δ.

7.3.1 Vertical equilibria – Kozai-Lidov equilibria: $\cos\omega = 0 \Leftrightarrow \omega = \pm\pi/2$

Let us observe that the addition of J_3 causes an asymmetry in the frozen orbit solutions not present before. Indeed, for $\omega = \pi/2$ the condition of equilibrium is given by

$$F_3(G,H,\gamma) + F_4(G,H,\gamma) + F_5(G,H,\delta) = 0 \tag{48}$$

whereas for $\omega = -\pi/2$ the condition of equilibrium is given by

$$F_3(G,H,\gamma) + F_4(G,H,\gamma) - F_5(G,H,\delta) = 0. \tag{49}$$

Then, for a small coefficient δ, the asymmetry is not important. However for a large value of this coefficient, the asymmetry could be important until the elimination of one of two equilibria.

7.3.2 Horizontal equilibria.

For horizontal equilibria, the condition of equilibrium ($\dot{G} = 0$) becomes:

$$F_1(G, H, \gamma) \sin\omega + F_2(G, H, \delta) = 0 \iff \sin\omega = -F_2/F_1 \overset{not.}{=} -\epsilon. \tag{50}$$

Then the "horizontal" equilibria appear for non-zero values of the pericenter $\omega = -\epsilon$ and $\omega = \pi + \epsilon$. The condition to obtain $\dot{\omega} = 0$ becomes:

$$F_3(G, H, \gamma) + F_4(G, H, \gamma)\epsilon^2 - F_5(G, H, \delta)\epsilon = 0, \tag{51}$$

that induces a shift in the equilibrium in G and ω variables with respect to the case "J_2 + third body". It is possible, in a similar way as before for J_2, to calculate the new values of the pericenter at the equilibria by solving the first equation (47). Then $\dot{G}$ vanishes for $\omega = \pm\pi/2$ (see previous section) or for

$$\omega = \arcsin\left(-\frac{\delta}{\gamma}\frac{5H^2 - G^2}{10G^6\sqrt{1-G^2}\sqrt{G^2-H^2}}\right) \tag{52}$$

with an existence condition on $\omega \in \mathbb{R}$ bounded by

$$H^2 = \frac{G^2}{5}\left(1 - 2G^5\gamma\left[5G^5\gamma(1-G^2) \pm 2\sqrt{5\left(1-G^2\right)\left(5G^{10}\gamma^2(1-G^2) + 4\delta^2\right)}\right]\right). \tag{53}$$

These solutions are equivalent to the equation (44) in Lara et al. (2010). If we insert this solution in the second equation (47), $\dot{\omega}$ vanishes for

$$H^2 = -\frac{\left(10G^7\gamma - 6\delta^2 \pm \sqrt{100G^{14}\gamma^2 + 20G^7\gamma\delta^2 + \delta^4 - 280\gamma^2G^{12}\delta^2}\right)G^2}{35\delta^2}. \tag{54}$$

Consequently with the method described in section 5.4 we can as well calculate the stability and the period of these equilibria.

7.3.3 Modifications of the phase space

For illustration, in Figure 14, we draw the contour plots of the new Hamiltonian for different values of J_3 (or for different values of δ). We see that when the δ coefficient increases (in absolute value), the vertical equilibrium goes down while the horizontal equilibrium goes below the "line $\sin\omega = 0$". We point out that, from some values of δ, the equilibrium $\omega = -\pi/2$ disappears (Fig. 14 right panel).

7.3.4 BepiColombo and other missions

At present time, the semi-major axis of the two orbiters (MPO & MMO) of the Bepi-Colombo mission are respectively equal to 3 394 km and 8 552 km. The MPO altitude corresponds to our (E') phase space where the eccentricity vector has a circular concentric motion. The MMO initial conditions, without thrust correction, leads to a crash onto the Mercury surface after 3 years. Based on our theory (and the underlying assumptions), we can choose another initial condition $a = 7\,355$ km and $e = 0.652$, that avoids forever the crash on Mercury and whose eccentricity vector is fixed.

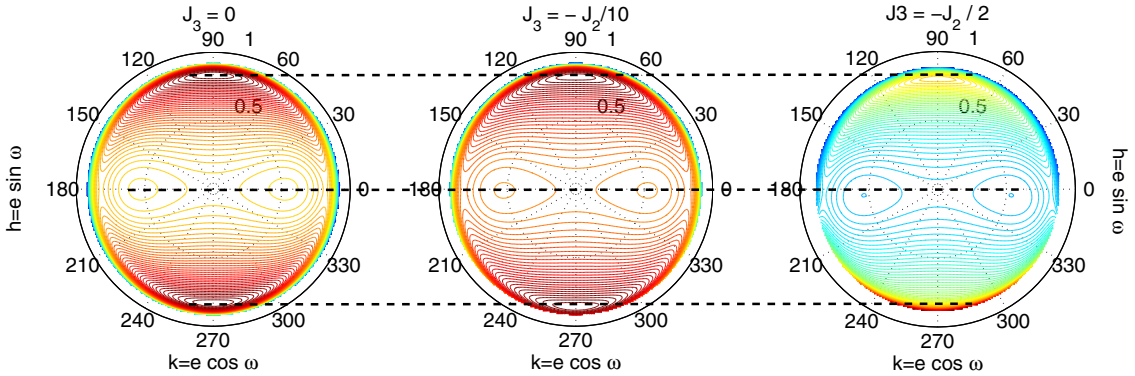

Fig. 14 Distortion of the phase space (for a Mercury's orbiter) due to J_3 effect. The initial conditions are $a = 5\,900$ km ($\gamma \simeq 0.66$) and $H^2 = 0.06$. J_3 (respectively δ) is equal to 0 (0), $-J_2/10$ (-0.041356) and $-J_2/2$ (-0.20678) in left, center and right panels.

8 Conclusions

The orbit dynamics of a space probe orbiting a planet or a natural planetary satellite has been investigated. The proposed model includes the effects of J_2 for the central body and the perturbation of the third body. We have developed a doubly averaged Hamiltonian and studied the location of the stable and unstable frozen orbits. Our method allows to have an analytical global approach to search all these equilibria and to compute the periods of the free librations at the equilibria. The analytical results have been checked and validated numerically by performing numerical integrations of the complete systems. Our theory is able to explain the behavior of our preliminary numerical investigations where the variation of the amplitude of the eccentricity is null and a separatrix is detected. The theory is general enough to be applied to a wide range of probes around any planet or any natural planetary satellite, provided that they respect the hypotheses used to obtain our Hamiltonian model.

We have shown the protection mechanism of the coefficient J_2 on the increasing of the eccentricity due to Kozai-Lidov effect. This mechanism is therefore able to produce a larger number of frozen orbits than those found in the only Kozai-Lidov problem. We have also explained the asymmetry of the frozen equilibria caused by the addition of the coefficient J_3. We have also brought to the light a local deformation of the Kozai-Lidov equilibria that appears at high eccentricity, high inclination and large value of γ.

These equilibria and their periods can be modified by including higher order terms of gravity field. However they will not change drastically the behavior of our phase space. Henceforth, the frozen orbits presented here provide good initial conditions to find periodic or frozen orbits in a osculating full model.

This theory provides analytical results to justify the choice of the intial semi-major axis and eccentricity of an orbiter for future missions around planets or planetray satellites.

Interested (separated) improvements would be to include the C_{22} coefficient of the central body or the inclination of the third body. In these cases the ascending node of

the probe would take place in the Hamiltonian leading to an extra degree of freedom i.e. 4D phase plots.

Acknowledgements The authors thank B. Noyelles and A. Albouy for fruitful discussions, the `IMCCE` team for their welcome and B. Meyssignac for initializing discussion.

Numerical simulations were made on the local computing ressources (*Cluster URBM-SYSDYN*) at the University of Namur (FUNDP, Belgium).

This work was partly supported by the fellowship *Concours des bourses de voyage de la Communauté Française de Belgique* obtained by Nicolas Delsate.

Finally, the authors thank the two referees for their suggestions that contributed to improve this paper.

References

Anderson J. D., Colombo G., Espsitio P. B., Lau E. L., and Trager G. B., The mass, gravity field, and ephemeris of mercury , Icarus, 71, 337-349, 1987.

Breiter S. and Elipe A., Critical inclination in the main problem of a massive satellite, Cel. Mech. Dyn. Astr., 95, 287-297, 2006.

Brouwer D. and Clemence G., Methods of Celestial Mechanics. Academic Press, 1961.

D'Hoedt S. and Lemaître A., Planetary long periodic terms in Mercury's rotation: a two dimensional adiabatic approach, Cel. Mech. Dyn. Astr., 101, 127-139, 2008.

D'Hoedt S., Noyelles B., Dufey J., and Lemaître A., A secondary resonance in Mercury's rotation, Cel. Mech. Dyn. Astr., 107, 93-100, 2010.

Dufey J., Noyelles B., Rambaux N., and Lemaître A., Latitudinal librations of Mercury with a fluid core, Icarus, 203, 1-12, 2009.

Farago F. and Laskar J., High-inclination orbits in the secular quadrupolar three-body problem, Monthly Notices of the Royal Astronomical Society, 401, 1189-1198, 2009.

Garcia D., de Pascale P. and Jehn R., Bepicolombo mercury cornerstone consolidated report on mission analysis. Tech. rep., MAO Working Paper No. 466, 2007.

Hairer E., Norsett S. and Wanner G., Solving ordinary differential equations I. Nonstiff problems. 2nd edition. Springer-Verlag, 1993.

Kozai Y., Secular perturbations of asteroids with high inclination and eccentricity. Astronomical Journal, 67, 591-598, 1962.

Lara M. and Russell R.P., Computation of a Science Orbit about Europa. Journal of Guidance, Control and Dynamics, 30, 259-263, 2007.

Lara M., Palacián J.F., Yanguas P. et al., Analytical theory for spacecraft motion about Mercury. Acta Astronautica, 66, 1022-1038, 2010.

Laskar J., Secular evolution of the solar system over 10 million years. Astronomy and Astrophysics, 198, 341-362, 1988.

Laskar J., Frequency map analysis and quasiperiodic decomposition, in Hamiltonian systems and fourier analysis: new prospects for gravitational dynamics, Benest et al. editors, Cambridge Sci. Publ., 99-129, 2005.

Lemaître A., Delsate N. and Valk S., A web of secondary resonances for large A/m geostationary debris, Cel. Mech. Dyn. Astr., 104, 383-402, 2009.

Lidov M.L., Evolution of the orbits of artificial satellites of planets as affected by gravitational perturbation from external bodies, 9, 719-759, Planet. Space Sci., 1962.

Lucchesi D. M. and Iafolla V., The Non-Gravitational Perturbations impact on the BepiColombo Radio Science Experiment and the key rôle of the ISA accelerometer: direct solar radiation and albedo effects, Cel. Mech. Dyn. Astr., 96, 99-127, 2006.

Paskowitz M. and Scheeres D., Orbit mechanics about planetary satellites, American Astronautical Society, 244, 2004.

Paskowitz M. and Scheeres D., Design of science orbits about planetary satellites: Application to europa. Journal of Guidance, Control and Dynamics, 29, 1147-1158, 2006.

Russell R.P. and Brinckerhoff A.T., Circulating eccentric orbits around planetary moons. Journal of Guidance, Control and Dynamics, 32, 424-436, 2009.

Russell R.P. and Lara M., Long-lifetime Lunar Repeat Ground Track Orbits. Journal of Guidance, Control and Dynamics, 30, 982-993, 2007.

Saleh L.A. and Rasio F.A., The stability and dynamics of planets in tight binary systems. The Astrophysical Journal, 694, 1566-1576, 2009.

San-Juan J., Lara M. and Ferrer S., Phase space structure around oblate planetary satellites. Journal of Guidance, Control, and Dynamics, 29, 113-120, 2006.

Scheeres D., Guman M. and Villac B., Stabillity analysis of planetary satellite orbiters: Application to the europa orbiter. Journal of Guidance, Control and Dynamics, 24, 778-787, 2001.

Seidelmann P. K. et al., Report of the IAU/IAG Working Group on cartographic coordinates and rotational elements: 2006. Cel. Mech. Dyn. Astr., 98, 155-180, 2007.

Standish E.M., JPL planetary and lunar ephemeris, de405/le405, JPL Interoffice Memorandum IOM 312.D-98-048, 1998.

Stoer J. and Bulirsch R., Introduction to numerical analysis, Springer-Verlag, New York, 1980.

Sturm C., Mémoires présentés par divers savants à l'Académie royale des Sciences de l'Institut de France, Vol.6, chap. Mémoire sur la résolution des équations numériques, 1835.

Tremaine S., Touma J. and Namouni F., Satellite dynamics on the Laplace surface, The astronomical journal, 1137, 3706-3717, 2009.